Haptic Simulation of Linear Elastic Media with Fluid Inclusions

Andrew H. Gosline, Septimiu E. Salcudean, and Joseph Yan
Department of Electrical and Computer Engineering
University of British Columbia, Vancouver, Canada
{andrewg, tims, josephy}@ece.ubc.ca

Abstract

We present a fast technique for simulating fluid-filled elastic objects with the Finite Element Method. By simulating the presence of fluid with hydrostatic fluid pressure, a quasi-static simulation of fluid can be achieved by applying a force boundary condition to the nodes on the fluid-elastic interface. Using a proportional feedback control algorithm, a relationship between the volume and pressure of the fluid structure can be maintained. Optimal parameters for the control algorithm are found by determining the response of the elastic system to changes in pressure. This approach has been shown to agree with experimental deformation data taken from a fluid-filled gelatin phantom. Combining linear FEM methods with matrix condensation techniques and the tuned proportional feedback control allows for the simulation of a fluid-filled elastic object at real-time haptic update rates.

1 Introduction

Haptic simulation of medical procedures is an active area of engineering research. Analogous to flight simulators for pilots, medical simulators allow students and doctors to learn and practice difficult procedures in a risk-free virtual environment with visual and force feedback. Procedures such as bone dissection [2], laparoscopy [6], [16], suturing [9], [26], and needle insertion [20] have been developed using a variety of techniques. One of the challenges in creating medical simulations is the real-time simulation of soft tissue. Many deformable methods have been developed and implemented in surgical simulations, usually treating tissue as an elastic material with either homogeneous or spatially varying stiffnesses. As medical simulators mature, however, more attention is required to model the human anatomy as accurately as possible. Human tissue contains many fluid-filled anatomical structures like glands, cysts, or blood vessels which are ignored if a deformable body is modeled using elastic techniques alone. In simulators where fluid is considered, such as laparoscopy [5] and mastiodectomy [2], it is done so only for graphical representation. Many common medical procedures occur in close proximity to fluid-filled organs, such as prostate brachytherapy. In this procedure the bladder is filled with a dilute contrast agent for CT imaging [12]. The prostate gland is located inferior to the bladder, so the bladder should be modeled as a fluid-filled elastic structure to make simulation of this anatomy as realistic as possible.

This paper describes a physically based method for simulating fluid-filled elastic objects that is fast enough for the high update rates required for haptics. Following a discussion of the related work, in Section 2, the modeling methods are described in Section 3. This includes a detailed problem description, an introduction to the FEM for linear elastostatic objects, a description of the fluid model employed, and a description of the numerical methods used to simulate the presence of fluid. Section 4 describes an experimental validation performed to compare deformation results from a fluid-filled gelatin phantom with results from a FEM simulation of the same phantom. Section 5 describes condensation techniques and presents an interactive haptic simulation of a fluid-filled elastic object. Finally, Section 6 presents conclusions and a discussion of future work.

2 Related Work

There has been a considerable amount of research done in the area of medical simulation that has been broken up into deformable models for haptics, FEM in haptics, and fluid modeling with the FEM.

2.1 Deformable Modeling for Haptics

Many methods have been used to describe the deformation of objects in haptic simulations. There are two different approaches, however, that make up the majority of this work. One is spring-mass particle methods and the other is continuum mechanics based elasticity methods.

Spring mass systems (SMS) use an interconnected network of spring-damper assemblies with point masses to simulate the deformation of a continuous body. Because the equations of motion are quite simple, SMS yields a relatively low computational cost [19]. d'Aulignac *et al.* [17] used SMS in a simulation of a human thigh, and Cotin *et al.* [16] used a combination of SMS and FEM to simulate laparoscopic surgery of a human liver. One of the benefits of SMS is that it is possible to change the topology of the mesh without a large computational penalty. This is not the case for most continuum mechanics based methods, and that is why Cotin *et al.* chose to couple SMS with FEM. There is, however, a major drawback to SMS. The deforma-

tion results are very sensitive to mesh topology and spring parameters. Much of the SMS related research is aimed at computing spring parameters and mesh topology such that the deformation matches a set of training data from elasticity or experimental measurements. For example, d'Aulignac *et al.* [17] used a two-step nonlinear least squares approach to match SMS parameters with a set of human thigh deformations and Bianchi *et al.* [10] used genetic algorithms to recreate SMS topology and parameters to mimic elastic deformations based on a FEM solution.

Continuum mechanics based methods, such as the FEM [20], [9], [11], [6], [35], [16] and Boundary Element Method (BEM) [28], [29], are based on elastic theory and tensor analysis so they can be parameterized accurately by physical constants such as Young's Modulus and Poisson's Ratio. This accuracy has made continuum mechanics methods, mostly the FEM, very popular for many disciplines of engineering. Section 2.2 will discuss the application of the FEM for haptic simulations.

In addition to SMS and continuum mechanics based methods, there exist many hybrid and composite deformable methods such as the Long Elements Method [4] and Chain-Mail [24]. For further reading about deformable methods for computer graphics and medical simulation, readers are referred to two survey papers by Gibson and Mirtich [25] and Delingette [19]. Due to the accuracy with which continuum mechanics based methods compute the deformation of elastic objects, the FEM is discussed for the remainder of this section.

2.2 Finite Element Methods in Haptics

There are methods with which FEM based elasticity can be accelerated to haptic rates. Cotin *et al.* [16] precompute the elementary deformations off-line and use linear superposition to render the deformations in real-time. BroNielsen and Cotin [11] use matrix condensation techniques to reduce the FEM stiffness matrix to include only those nodes that are on the surface of the deformable body. In a similar approach, Berkley *et al.* use banded matrix algorithms to precompute the stiffness matrix for a suturing simulator, DiMaio and Salcudean [20] use condensation techniques in an interactive needle insertion simulator, and Basdogan and Srinivasan [6] used condensation in a laparoscopy simulator. Instead of matrix condensation, an operation that is only applicable to linear systems, Zhuang and Canny [35] used an interpolation scheme to allow fast haptic update rates in their simulation of elastic objects with a nonlinear strain FEM formulation.

The fastest and most flexible of the formulations used in prior work is the linear elastostatic FEM with condensation. The limitations associated with this method are that the linear elastic strain tensor is only accurate for small strains, of order 1% [25], and that only a linear stress-strain relationship can be accommodated. Linear elastostatic FEM has a huge advantage over any nonlinear method because matrix condensation can greatly reduce the number of required computations. With present computing hardware constraints and haptic update requirements of approximately 500 Hz, linear elastostatic FEM is a logical choice for the development of medical simulators.

2.3 Fluid Modeling with the Finite Element Method

There are several ways that the FEM can be used to model fluid-solid interaction. Bathe *et al.* [7] use an Eulerian-Lagrangian formulation to couple Navier-Stokes fluid flow with structural analysis. This formulation requires that the fluid boundary be coupled to the solid by integrating the nodal velocities over a timestep. This results in a matrix that is asymmetric and poorly banded, requiring the use of iterative solvers like the Newton-Raphson method. As a result, this formulation is far too computationally intensive for real-time applications.

In recent work, Baxter and Lin [8] used Navier-Stokes based fluid mechanics to simulate haptic interaction with viscous fluid in a painting simulation. In their work, using a grid size of 64×64 nodes, the simulation can run at approximately 70 Hz, so a low pass filter is required to stabilize the interaction. This work illustrates how computationally intensive Navier-Stokes based fluid dynamic analysis is. For the goal of rendering fluid-filled elastic objects in medical simulators, where the accurate flow simulation is not as important as the resulting elastic deformation, a simpler and less computationally intensive fluid analysis should be used.

Donangun *et al.* [22] used irrotational elastic elements for static and dynamic analysis of rigid water tanks. To decouple the fluid elements from the elastic elements and enforce the 'slip' condition at the fluid-elastic interface, short stiff trusses were used. Unfortunately, these truss elements only decouple the interface for deformations of the same magnitude as their length, and hence this method is unsuitable for medical simulators where large deformations are required.

De and Srinivasan [18] used a nonlinear FEM formulation to model human organs as thin elastic walls enclosing incompressible fluid. Due to the nonlinear formulation, this method cannot be accelerated with matrix condensation because it requires an iterative solution on the elastic system. Furthermore, this method's applicability to real-time simulation is based solely on the reduction in dimensionality. That is, to represent a volumetric deformable object using only a thin surface reduces the complexity from $O(n^3)$ to $O(n^2)$. If a body of elastic solid is required in addition to a thin walled organ, this reduction in dimensionality is no longer achieved, and the solution time will likely be too large for real-time applications.

3 Method

Consider an arbitrarily shaped elastic body Ω, as illustrated in Figure 1. This body may contain pockets of fluid, Ω_{f1} and Ω_{f2}, each of which has a *quasi-static* relationship between the pressure and volume that is known, shown in Figure 1(a). This body may also contain regions in which

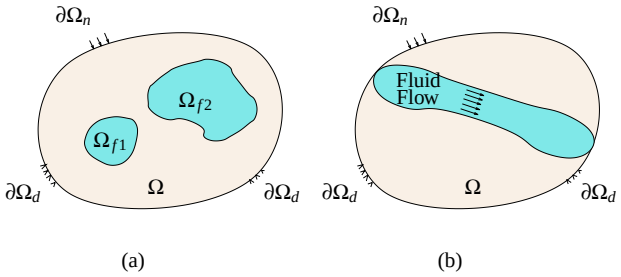

Fig. 1. Fluid Filled Structures Enclosed in Elastic Media

fluid moves with known flow properties, shown in Figure 1(b). The exterior boundary, $\partial\Omega$, may be constrained by a geometric Dirichlet boundary condition ($\partial\Omega_d$), and tractions may be imposed by a Neumann boundary condition ($\partial\Omega_n$). The problem is to compute the resulting body deformations and forces at a rate that is fast enough for haptic simulation which requires force updates to be approximately 500 Hz. The remainder of this section describes a method that achieves this goal.

3.1 Finite Element Method for Linear Elasticity

The Finite Element Method for homogeneous elastostatic material is used to describe the deformation of elastic bodies in this work. The Generalized Hooke's law states:

$$\sigma = D\varepsilon \tag{1}$$

where σ and ε are the stress and strain vectors on a body respectively, and D is the elasticity matrix. For the case of isotropic materials, the elasticity matrix can be parameterized by two independent elasticity variables, Young's Modulus, E, and Poisson's Ratio, ν. Young's Modulus is a measure of the material's stiffness, and can be determined experimentally from the slope of a stress vs. strain curve. Poisson's Ratio describes the compressibility of the material and ranges from 0, for very compressible materials, to 0.5, for incompressible materials.

The strain energy of a linear elastic body, Ω, can be computed by:

$$E_{strain} = \frac{1}{2}\int_{\Omega} \varepsilon^T \sigma \, dx \tag{2}$$

(2) can be expressed as a function of deformation by substituting $\sigma = D\varepsilon$ and $\varepsilon = Bu$ where B is the Linear Strain Tensor [13] and u is the displacement vector.

$$E(u)_{strain} = \frac{1}{2}\int_{\Omega} (Bu)^T DBu \, dx \tag{3}$$

Static equilibrium between deformation energy and external force is achieved when the first variation of $E(u)_{strain}$ vanishes. This occurs when $\delta E(u)_{strain} = 0$, which corresponds to the potential energy of the system reaching a minimum value [11]. For a finite element, Ω_e:

$$\delta E^e(u)_{strain} = 0 = \int_{\Omega_e} B_e^T DB_e \underline{u_e} \, dx - \underline{f_e} \tag{4}$$

where $\underline{f_e}$ and $\underline{u_e}$ are the force and displacement vectors that have been discretized over the element, and B_e is a constant matrix (for a triangular or tetrahedral element) that uses the natural co-ordinates of a triangle to interpolate nodal displacements, as defined in [11]. (4) is integrated over each discrete volumetric element to generate a stiffness matrix for each element. A stiffness entry from each element is added to the global stiffness matrix, K, which creates a system of $3n$ (for a 3D object) linear equations that describes the deformation of each of the n nodes by the linear system:

$$\underline{f} = K\underline{u} \tag{5}$$

where $\underline{u}$ and $\underline{f}$ are the displacement and force vectors, ordered based on node number such that:

$$\underline{f} = \left[\, f_{1x}, f_{1y}, f_{1z}, f_{2x}, \ldots, f_{nx}, f_{ny}, f_{nz} \,\right]^T \tag{6}$$

$$\underline{u} = \left[\, u_{1x}, u_{1y}, u_{1z}, u_{2x}, \ldots, u_{nx}, u_{ny}, u_{nz} \,\right]^T \tag{7}$$

3.2 Fluid Simulation with Hydrostatic Pressure

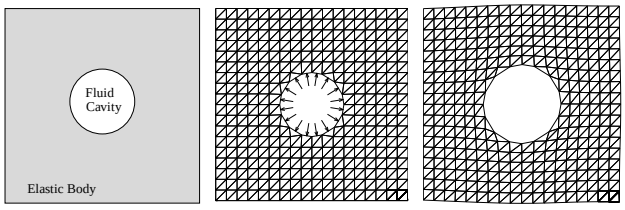

(a) Elastic Body with Fluid Inclusion

(b) FEM Discretization with Pressure Normals

(c) Deformed After Pressure Applied

Fig. 2. Elastic Body Discretized with 2D Triangular Finite Elements

In this work, fluid is modeled using static fluid analysis, where the only fluid quantity is hydrostatic fluid pressure. For simplicity, this pressure is assumed constant over the fluid volume, neglecting gravitational effects. This assumption is valid for small enclosed fluid volumes, as the pressure gradient varies linearly with depth. For fluid flow, however, gravitational effects would need to be computed *a priori* and included with a *quasi-static* fluid pressure to volume relationship such as pulsing blood pressure to model vascular flow.

For FEM analysis, fluid pressure is treated as a constant distributed force over each element, such that the effective force on a fluid-elastic boundary element, $\underline{F_e}$, is computed by:

$$\underline{F_e} = \int_{A_e} P \, dA = P \, A_e \hat{n}_e \tag{8}$$

where P is the fluid pressure, A_e is the area of the element, and $\hat{n}_e$ is the outward unit normal of the element. $\underline{F_e}$ is used as a force boundary condition for each of the fluid exposed nodes to simulate the presence of a fluid. Figure 2(b) illustrates a discretized elastic body with fluid normals on the

boundary. Figure 2(c) shows the elastic body after a positive pressure is applied to the cavity. Note how the fluid cavity has enlarged and the elements on the fluid boundary are stretched.

In order to simulate the presence of a fluid inside the cavity, an appropriate pressure to volume relationship is used to accommodate different fluid geometries. For instance, blood flow could be simulated using a time varying pressure relationship that uses typical human blood pressures and heart rates to govern the fluid related deformation. While this is a coarse approximation to the complex flow that actually occurs in the vascular system [23], it will indeed be fast enough to solve at haptic update rates. On the other hand, an incompressible fluid-filled cavity exhibits a constant volume regardless of the body deformation. In this case, the fluid pressure will change such that volumetric strain is zero. The challenge is to compute this incompressible fluid pressure and simulate the fluid-filled object at haptic update rates. Because an incompressible fluid-filled cavity is both a useful and challenging, this is the fluid model that is concentrated on for the remainder of the paper. However, the methods described in the following sections use general principles that would work for other types of fluid-elastic systems like blood vessels.

3.3 Incompressible Fluid-Filled Cavities

To simulate an incompressible fluid-filled cavity, it is necessary to compute the internal pressure such that the cavity volume remains constant. It is possible to add the deformation energy of the fluid to the Finite Element formulation, but the resulting relationship is nonlinear [34]. In order to preserve the linearity of the FEM formulation, the fluid simulation should be abstracted from the elastic simulation so that linear system optimization techniques are still applicable. The method by which this is done is to iteratively change the fluid pressure until the cavity volume is conserved. Figure 3 illustrates the algorithm using a square fluid-filled cavity enclosed in an elastic body. In Figure 3(a), the object has no external load, and the internal cavity pressure is the same as the external pressure. In Figure 3(b), an external force has been applied, but still the cavity pressure is the same as external pressure, so the object has deformed and the cavity volume has decreased. In Figure 3(c), an external force has been applied and pressure has been added to the cavity such that the cavity volume is the same as in the rest case. Note that the cavity in Figure 3(c) has bulged to maintain a constant volume.

For real-time simulation of incompressible fluid-filled structures, a fast numerical method is required to compute the appropriate fluid pressure such that volume is conserved. The relative volume error is defined as:

$$Error_i = 1 - \frac{V_i}{V_o} \tag{9}$$

where V_i is the volume of the deformed cavity and V_o is the original volume. To minimize the error within a predefined

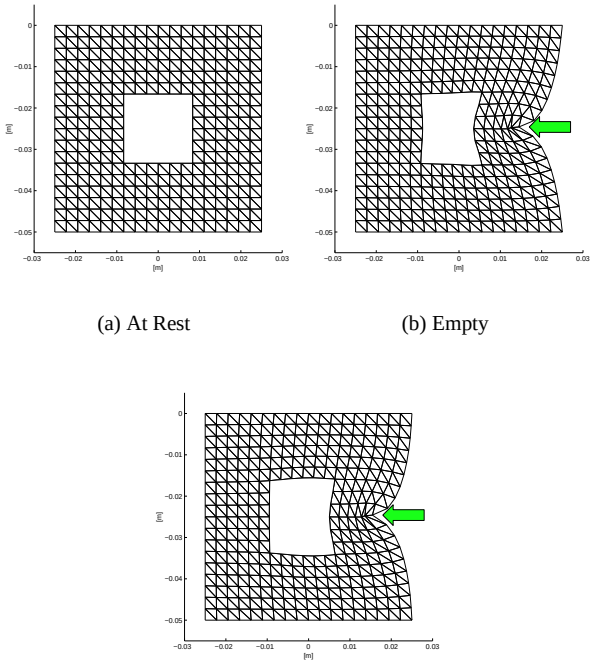

(a) At Rest (b) Empty

(c) Fluid

Fig. 3. Example of FEM Algorithm

tolerance to zero, a proportional pressure update law is used, such that:

$$P_{i+1} = P_i + K_p Error_i \tag{10}$$

where K_p is a constant gain.

The performance of this update law is dependent on the tuning of K_p as the relationship between the cavity pressure and volume varies with the stiffness and geometry of the elastic object. As a result, a method for tuning the update law to a given elastic object is required.

Given an elastic object with a cavity inside, such as Figure 3, an object-specific pressure vs. volume curve can be generated by changing the pressure inside the cavity and computing the volume of the cavity at each pressure. Figure 4 shows the pressure vs. volume curve for the elastic object in Figure 3, that is a $5 \times 5 \times 1.2\text{cm}^3$ block with a Young's Modulus of 34 kPa and Poisson's Ratio of 0.35. The cavity pressure is varied from a 30% reduction in volume to a 30% increase in volume, shown by Figures 4(b) and 4(c).

From Figure 4(a) it can be seen that the pressure vs. volume curve for this object is nonlinear. However, a least squares line fit to the curve provides a very good approximation over the 30% range. The slope of this line represents a linear approximation to the cavity pressure to volume relationship of the elastic object, and is therefore an excellent choice for K_p. With this slope as an optimal value for K_p, performance of the update law is good. Strains of order 0.3% to 15% solve to a volume tolerance of 1% in a maximum of 1 pressure update. For the relatively simple fluid-filled elastic

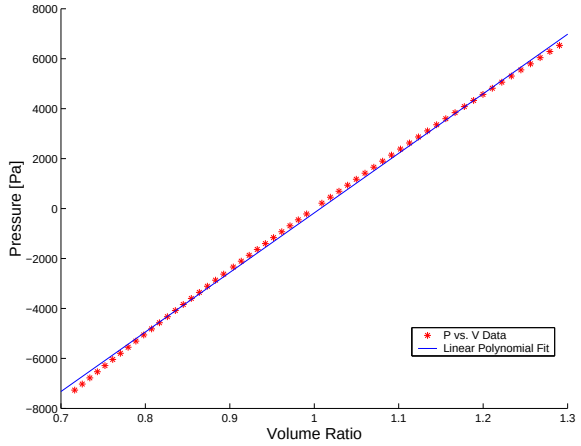

(a) Pressure vs. Volume Curve

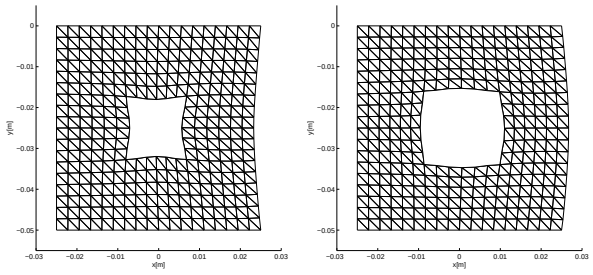

(b) Cavity at 70% Volume (c) Cavity at 130% Volume

Fig. 4. Pressure vs. Volume of the Cavity in a Simulated Elastic Body

objects presented in this paper, the slope was used as K_p with good results. However, if the pressure vs. volume cannot be approximated well with a single line fit, a piecewise line approximation or a line search algorithm such as the golden section rule could be used.

3.4 Volume Calculation

It is necessary to compute the volume of the cavity for each iteration numerically. The computation of the area of a 2D polyhedral shape is computed by summing the areas of all of the trapezoids in order of connectivity. (11) expresses the sum of each trapezoid around the contour. It is important that the order be consistent so that trapezoids on the upper surface contribute positively to the area, and trapezoids on the lower surface contribute negatively.

$$A = \sum_{i=1}^{n} A_i = \sum_{i=1}^{n} h_i dx_i = \frac{1}{2}\sum_{i=1}^{n} x_i y_{i+1} - x_{i+1} y_i \qquad (11)$$

Computing the volume of an arbitrary 3D object that is defined by a polyhedral surface, and is not necessarily convex is not as trivial as in 2D. Mirtich [30] developed a fast method for computing polyhedral mass properties based on a surface representation that uses three steps to reduce a volume integration to a set of line integrals over each face. His method is used to compute the volume of the fluid cavity in the 3D cases.

The method first uses the Divergence Theorem to reduce a volume integral of a vector field F over a volume $\mathcal{V}$, to an integral over a closed surface, $\partial\mathcal{V}$ by:

$$\int_{\mathcal{V}} \nabla \cdot F dV = \int_{\partial\mathcal{V}} F \cdot \hat{n}\, dA \qquad (12)$$

If $F = [x, 0, 0]$, then $\nabla \cdot F = 1$, and the left side of (12) reduces to $\int_{\mathcal{V}} 1\, dV = V$. The volume of the closed surface composed of discrete faces, $\mathcal{F}$ can be computed by:

$$V = \sum_{\mathcal{F} \in \partial\mathcal{V}} \hat{n}_x \int_{\mathcal{F}} x dA \qquad (13)$$

Next, the integral over a face, $\mathcal{F}$, in (x,y,z) is reduced to a projection integral over the bounded region, Π, in the (α,β) plane where (α,β,γ) is a right-handed permutation of (x,y,z) chosen so that the projection onto the plane is maximized to minimize numerical errors. A plane in (α,β,γ) space is defined by:

$$\hat{n}_\alpha \alpha + \hat{n}_\beta \beta + \hat{n}_\gamma \gamma + w = 0 \qquad (14)$$

So, the face integral is reduced to a projection integral by:

$$\int_{\mathcal{F}} f(\alpha,\beta,\gamma)\, dA = \frac{1}{\hat{n}_\gamma} \int_{\Pi} f(\alpha,\beta,h(\alpha,\beta))\, d\alpha d\beta \qquad (15)$$

where $h(\alpha,\beta) = \frac{1}{-\hat{n}_\gamma}(\hat{n}_\alpha \alpha + \hat{n}_\beta \beta + w)$. Finally, the projection integral is reduced to a set of line integrals by Green's Theorem in a Plane, which is a 2D version of the Divergence Theorem.

$$\int_{\Pi} \nabla \cdot H\, dA = \oint_{\partial\Pi} H \cdot \hat{m} ds \qquad (16)$$

where $\hat{m}$ is the outward normal of each line segment of length s, that make up the bounded region, Π, in a counter clockwise order. It is interesting to note that (16) reduces exactly to (11), so the 2D area calculation presented previously is an intuitive implementation of Green's Theorem in a Plane.

4 Experimental Validation

To validate that the combination of hydrostatic fluid pressure with linear FEM analysis predicts deformations in a physically realistic manner, an experimental validation has been performed. A fluid-filled gelatin phantom, with known material properties, was deformed with a known load while the top surface was tracked with a digitizing pen and the contour of the fluid cavity was imaged using ultrasound. The data from these experiments were then compared to an FEM analysis of the experiment. In this section, each of the experimental components is discussed in detail, and results are presented.

4.1 Phantom

There exist a variety of materials that are suitable for construction of tissue phantoms. For experimental validation of the fluid modeling method described in the previous section, however, a material that exhibits linear elastic properties is required. Hall *et al.* [27] tested the material properties of agar and gelatin for elastography. According to their study, gelatin is linear elastic to approximately 10% strain, while agar exhibits nonlinear elastic properties. Due to the ease of use and linear elastic properties, gelatin was chosen as the phantom material for this work.

Gelatin phantoms were constructed by dissolving 13% B-Type Sigma Gelatin from bovine skin in heated de-ionized water, then pouring the mixture into a mold and cooling until the gel is set. To add a fluid enclosure to the phantom, a fluid-filled latex glove fingertip was cast inside the gelatin. This required that the glove tip was suspended by threads in the mold prior to pouring the gelatin. These threads were then carefully removed after the phantom had set. Care was taken to make sure the fluid-filled glove tip was as compliant as possible, so its effect could be neglected from the FEM analysis. The glove fingertip was filled with a 10% glycerol-de-ionized water mixture.

To image the fluid pocket shape with ultrasound, there must be sufficient contrast between the fluid pocket and the surrounding gelatin. A byproduct of ultrasound imaging is "speckle", which is the result of random sound waves that have been deflected by reflective objects in the sample. Gelatin alone, however, does not produce "speckle", and if the fluid-filled phantom were made with gelatin alone, there would be very little contrast between the fluid and elastic regions. To generate sufficient "speckle", small scattering objects were added to the gelatin mixture. According to the results found by Rickey *et al.* [31], 3% SigmaCell cellulose was added to the gelatin mixture prior to pouring the mold. The cellulose does not dissolve in the gelatin mixture, so once mixed into suspension, the gel was cooled immediately to minimize settling. The resulting contrast between the fluid and gelatin is evident in the ultrasound images in Section 4.5.

The material properties of the gelatin/cellulose mixture are required as input parameters for the FEM analysis. According to Sciarretta *et al.* [33], gelatin is nearly incompressible, with a Poisson's Ratio of approximately 0.485. The Young's Modulus of the mixture can be determined experimentally using a parallel plate compression test. A block of the gelatin/cellulose mixture of known size was compressed over a series of known compressive displacements with a motion stage, while a force sensor measured the compressive force at each displacement. Figure 5(a) shows the apparatus. From the displacement vs. force data a stress vs. strain plot was generated, as shown in Figure 5(b). The gelatin/cellulose mixture was found to have a linear Young's Modulus of approximately 15.2 kPa up to approximately 15% strain.

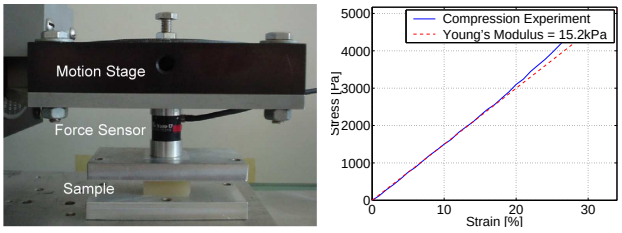

(a) Parallel Plate Compression Apparatus

(b) Compression Results

Fig. 5. Ultrasound Phantom Material Properties

4.2 Experimental Apparatus

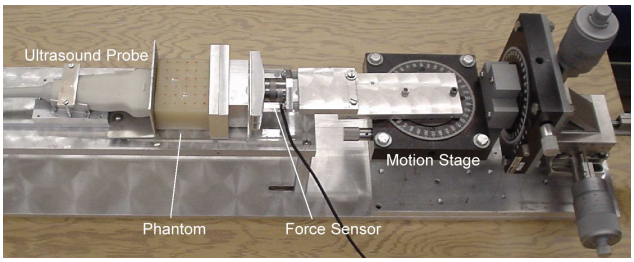

(a) Apparatus

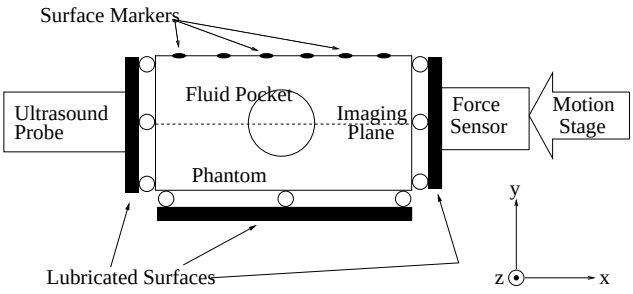

(b) Schematic

Fig. 6. Experimental Apparatus

The experimental apparatus is shown in Figure 6(a) and an apparatus schematic diagram is shown in Figure 6(b). On the left is a 12 MHz, 40 mm linear array ultrasound probe rigidly mounted to a full length aluminum base. This probe is connected to an Ultrasonix 500 ultrasound imaging system with the research software package [15]. The probe is mounted flush to a vertical plate that constrains the phantom and allows the fluid inclusion to be imaged. In the middle is the phantom, with the top surface and tracking markers visible. To the right of the phantom, an ATI Nano25 force/torque sensor is mounted to a Newport 3DOF motion stage. The motion stage is rigidly mounted to the same aluminum base as the ultrasound probe to ensure all compressive force im-

parted by the motion stage is transfered directly to the phantom.

4.3 Digitizing Pen

3D locations of regularly spaced markers on the top surface of the phantom were sampled using a digitizing pen that uses the OptoTrak 3020 tracking system. The digitizing pen consists of 4 OptoTrak markers that are rigidly attached in a "T" pattern to a sharp pointer. Once the pen has been calibrated, using the method described by Rohling *et al.* [32], the digitizing pen can be used to sample marker co-ordinates with sub-millimeter accuracy. The largest source of error in tracking the markers by hand comes from the manual positioning of the pen tip.

4.4 Finite Element Simulation

To re-create the experiment with a FEM simulation, a 3D FEM mesh of the phantom is required. To generate such a mesh, a series of parallel ultrasound images were taken at 2 mm increments with the 3DOF motion stage. To take this set of ultrasound images, the apparatus was slightly modified from the configuration shown in Figure 6(a). The force sensor and impactor were removed from the motion stage, and the ultrasound probe was moved closer to the motion stage. The phantom was then placed on the stage so that it could move vertically relative to the probe with known displacements, and a series of parallel images could be taken. Each of the resulting images was hand segmented for the location and radius of the fluid inclusion using a digital caliper and the image scale factor. This set of images was taken perpendicular to the long axis of the fluid pocket so that in each image the contour of the fluid inclusion is circular. Next, a regularly spaced mesh of the phantom cast filled with tetrahedral elements was created. Elements that contain a node that is inside the fluid inclusion were removed from the mesh. Then the boundary of the inclusion was shifted to match the center point and radius measurements. The resulting mesh had 1328 nodes, which yields a 3984×3984 stiffness matrix. A Young's Modulus of 15.2 kPa and a Poisson's Ratio of 0.485, from [33], were used as the elasticity parameters for the 4 node, linear strain tetrahedral elements.

The motion stage imparts a known displacement on the phantom. As such, the boundary condition that must be applied to the FEM model should also be a displacement. To achieve this, a boundary condition change [20], is necessary. After boundary condition changes have been performed on K^{-1}, the notation changes to $x = K^{-1'}y$ where x replaces u and y replaces f because what used to be homogeneous displacement and force vectors now contain a mix of displacement and force entries. This notation is used in the remainder of the paper to indicate that boundary condition changes have been applied.

As described in Section 3.1, the elastostatic FEM formulation used in this work only considers an energy balance between deformation and external force. It is therefore required that the elastic object be sufficiently constrained in all degrees of freedom such that the body can only deform, it cannot move. If the object is not sufficiently constrained, there will be no unique solution, and K is singular. The phantom is constrained horizontally between the two plates, and vertically along the bottom surface, shown in Figure 6(b). With these constraints, the phantom is sufficiently constrained in both X and Y, but not in Z. To ensure a unique solution, a node on the ultrasound plate at the bottom of the phantom was constrained in Z.

4.5 Results

The phantom was deformed with three displacements, 3 mm, 6 mm, and 9 mm. For each deformation, an ultrasound image and surface data were collected. Figure 7 shows the ultrasound images of the fluid inclusion in comparison with the FEM predicted shape. Nearest-neighbor was used as the interpolation scheme to interpolate the node positions from the FEM simulation, and the results were scaled and translated to match the images. The top of each image corresponds to the side of the phantom that is held in contact with the ultrasound probe, while the bottom of each image is in contact with motion stage (visible as the bright horizontal line). The FEM solution predicts the contour of the fluid pocket quite well. The largest error occurred in the 9 mm deformation case where the top left of the contour was predicted by FEM to move approximately 3.3 mm while the ultrasound contour moved 3.71 mm. Note that the contour of the pocket and the nodes of the pocket are not perfectly aligned even in the undeformed case, which is likely caused by the circular contour assumption in hand segmentation.

Figure 8 shows a comparison between deformations from the markers and the FEM simulation. The trends are consistent between the experimental and simulated data. The markers near the displacement surface move considerably, while the markers near the fixed surface move only slightly. Markers in the center of the phantom compress almost vertically, with very little horizontal expansion, while markers near the edges show considerable horizontal expansion.

Figure 9 shows the locations of markers compared with the locations of the corresponding FEM nodes for the various deformation cases. Marker positions are registered with the FEM data using a 2-step least squares approach. The data were first fit to a plane for the undeformed case using the method described by An *et al.* [3]. Then, linear least squares was used to compensate for rotation and scaling [14]. Despite the errors introduced by hand tracking the markers on a soft, deformable object, the FEM simulation agrees with the experimental data on the top surface. The "o" symbols in the figure are approximately 1 mm in diameter, which is representative of the estimated 1 mm error from hand tracking. The majority of the node positions are within the "o", indicating that the data agree with the simulation within the error of the experiment.

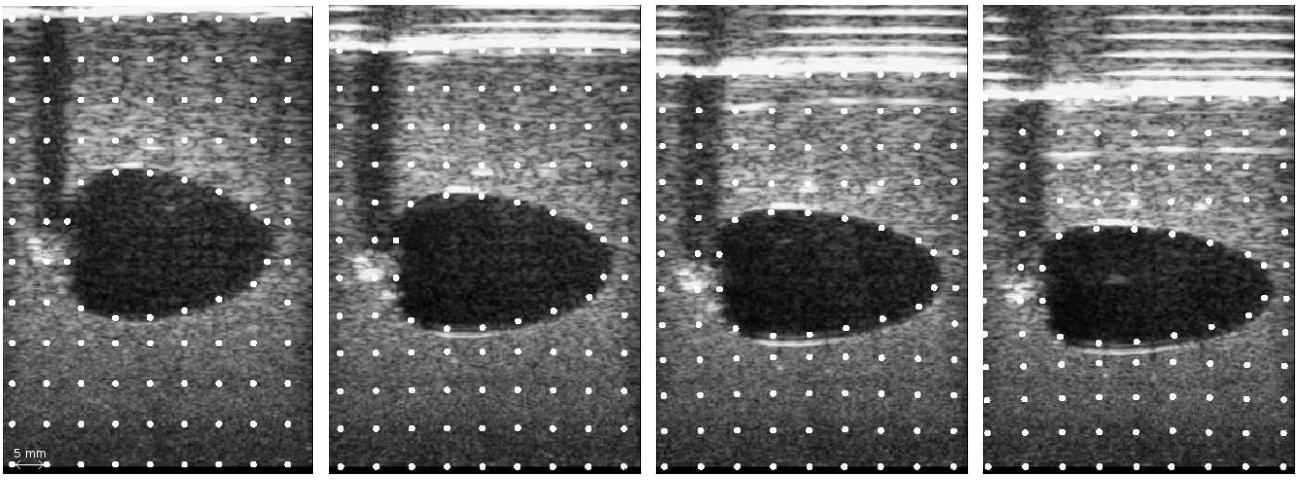

(a) No Load (b) 3 mm Displacement (c) 6 mm Displacement (d) 9 mm Displacement

Fig. 7. Ultrasound vs. FEM Contours

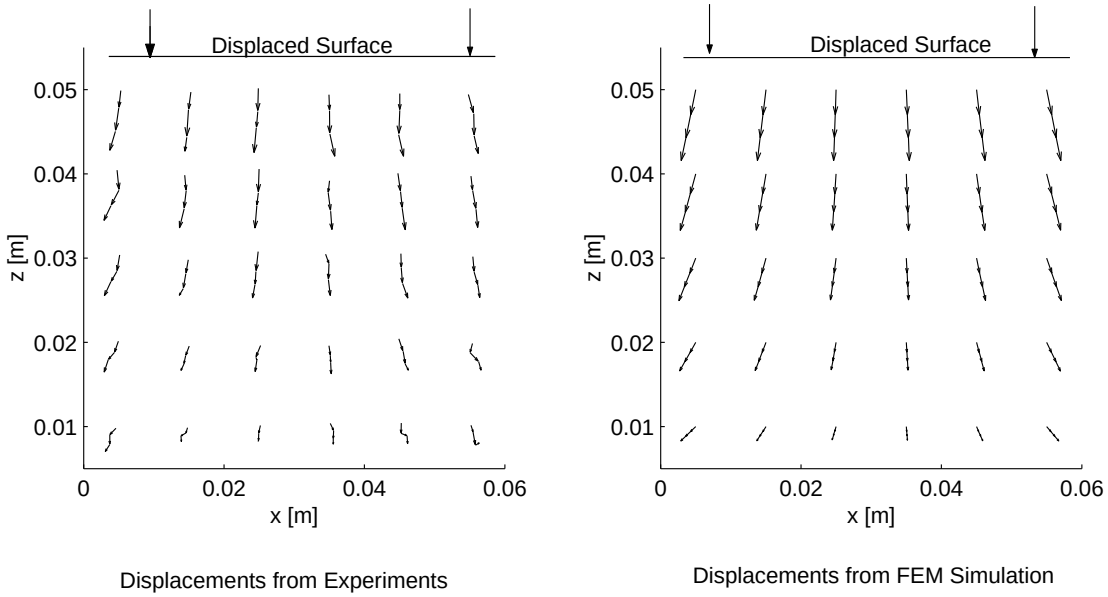

Fig. 8. Top Surface Marker Displacements vs. FEM Displacements

5 Haptic Simulation

Matrix condensation is an important component of the approach that allows fluid-filled elastic structures to be simulated at typical haptic update rates. This section will outline matrix condensation, then describe an implementation of the algorithm presented in Section 3.

5.1 Matrix Condensation

The technique that allows FEM simulation of elastic objects to run at typical haptic update rates is matrix condensation. Consider the linear FEM system:

$$K\underline{u} = \underline{f} \tag{17}$$

In typical FEM systems, the load vector $\underline{f}$ is known, and the displacement vector $\underline{u}$ is unknown. Also, because many nodes are located within the volume of the elastic solid and are not subject to external force, the load vector is typically sparsely populated. Matrix condensation takes advantage of this sparsity by precomputing for nodes that do not have a force applied to them, referred to as "free" nodes. The result is a system that computes only the deformation of non-free nodes exactly as if the full system was solved [11].

In the case of an implicit linear system, such as (17), the system can be condensed using Gaussian Elimination [13]. When the implicit system is condensed, however, changes to the system are computationally expensive because the sys-

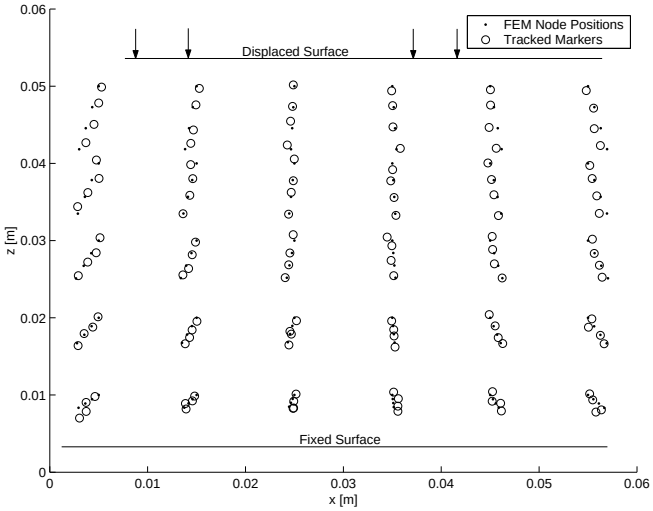

Fig. 9. Error Plot from Top Surface Tracking

tem needs to be re-condensed. This is not the case, however, for the explicit system:

$$\underline{u} = K^{-1}\underline{f} \tag{18}$$

The explicit system is not typically used in engineering applications due to long inversion time and numerical errors due to inversion [11]. However, for the application of real-time haptics, neither of these drawbacks outweigh the benefit that the explicit system can be condensed trivially on the fly. For example, the system

$$\begin{bmatrix} u_1 \\ u_2 \\ u_3 \\ u_4 \end{bmatrix} = \begin{bmatrix} K_{11}^{-1} & K_{12}^{-1} & K_{13}^{-1} & K_{14}^{-1} \\ K_{21}^{-1} & K_{22}^{-1} & K_{23}^{-1} & K_{24}^{-1} \\ K_{31}^{-1} & K_{32}^{-1} & K_{33}^{-1} & K_{34}^{-1} \\ K_{41}^{-1} & K_{42}^{-1} & K_{43}^{-1} & K_{44}^{-1} \end{bmatrix} \begin{bmatrix} f_1 \\ f_2 \\ f_3 \\ f_4 \end{bmatrix} \tag{19}$$

can be reduced to:

$$\begin{bmatrix} u_1 \\ u_3 \end{bmatrix} = \begin{bmatrix} K_{11}^{-1} & K_{13}^{-1} \\ K_{31}^{-1} & K_{33}^{-1} \end{bmatrix} \begin{bmatrix} f_1 \\ f_3 \end{bmatrix} \tag{20}$$

if f_2 and f_4 are free.

5.2 Interactive Simulation of a Fluid-Filled Structure

Using the needle insertion simulator described by DiMaio and Salcudean [20] as a basis, an interactive simulation of an incompressible fluid-filled elastic object was created. This 2D simulator uses the 3DOF planar pantograph as an interface [21]. The simulation architecture consists of two PCs that communicate over a UDP socket connection. The first PC is a 2.0 GHz Pentium 4 that runs VxWorks at a fixed update rate of 512 Hz. This PC is responsible for device control, dynamics, and simulation. The second PC runs Windows and is responsible for graphics, which is updated at approximately 30 Hz. Figure 10(a) shows the simulation in use, while Figures 10(b) and 10(c) show a close up of the graphics output when the fluid pocket is under tension and compression respectively. The elastic object in the haptic simulation is identical to the one discussed in Section 3.3, so the pressure update gain that was determined numerically in Section 3.3 was used. The scope output at the bottom of Figures 10(b) and 10(c) displays the relative volume of the fluid pocket in real-time. The scope output showed that the volume did not deviate from the initial volume by more than 0.1%, and the pressure calculation did not require more than 1 iteration. A short video clip is available online [1].

The algorithm for an incompressible fluid pocket is as follows:

1. OFFLINE: Create a FEM system matrix, K_{global}^{-1}, and initially condense this matrix to include only the nodes that exist on the fluid boundary, $K_{working}^{-1}$. Compute the original volume of the fluid pocket, V_o, and compute the normal directions to the fluid cavity. Precompute the optimal gain, K_p.
2. As the needle comes in contact with the tissue, add the new node's appropriate row and column entries from K_{global}^{-1} to $K_{working}^{-1}$. Perform the necessary boundary condition changes and local co-ordinate system changes, as outlined in [20]. Add the needle force contribution to the vector y.
3. Compute the product $x = K_{working}^{-1} y$, then the volume of the fluid pocket, and the error term $Error_i = 1 - \frac{V_i}{V_o}$.
4. If the error is not within a 0.1% tolerance to zero, update the pressure by $P_{i+1} = P_i + K_p Error_i$. Add the force contributions from pressure to the y vector. Re-iterate from step 3.
5. Integrate needle forces, output hand force to haptic device, send node positions to graphics display.

5.3 Computational Requirements

Condensation allows a fluid-filled volumetric object to be represented by a contact area and a fluid interface surface. As a result, the size of $K_{working}^{-1}$ scales $O(n^2)$ with the number of nodes on the fluid boundary. The complexity of $K_{working}^{-1} y$ also scales $O(n^2)$, while the volume calculation scales $O(n)$. The result of this scaling is that a large fluid-filled elastic body can be simulated while only the nodes that are either in contact with the surgical tool or on the fluid-elastic boundary need to be computed in the haptic loop.

A computational timing experiment using a 2.4 GHz Pentium 4 PC with 512 Mb of memory was performed to investigate the update rates possible on current hardware. The 3D simulation of the ultrasound phantom, as described in Section 4, was condensed to include the nodes on the fluid-elastic interface (80 nodes) and 2 nodes on the exterior surface to simulate a tool in contact with the phantom. This condensed system is consistent with what would be required in the haptic loop of a haptic simulation of the experimental phantom, and the same method for computing the optimal control gain as described in Section 3.3 was used. Using the Intel C++ 7.0 optimized compiler, this 82 node condensed system could be solved with 1 pressure iteration at an update rate of approximately 3000 Hz. It is important to note, however, that this timing experiment did not address the compu-

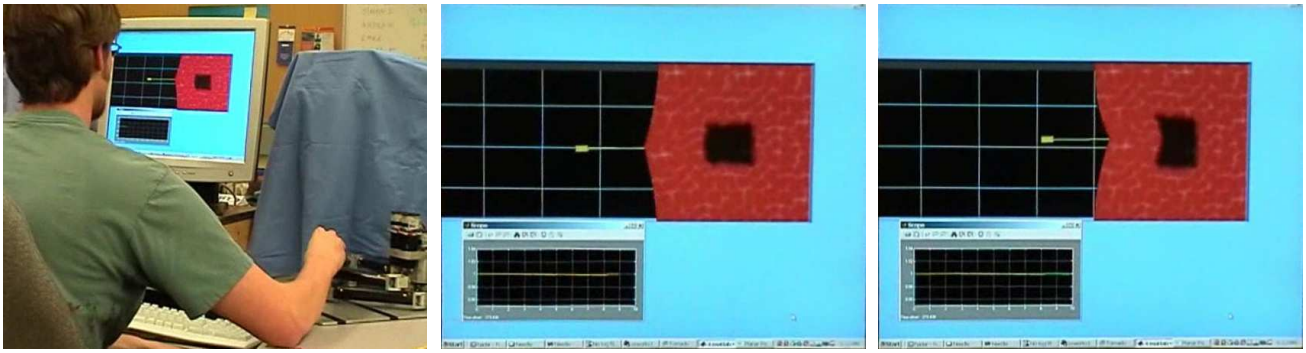

(a) Haptic Simulation Setup (b) Pocket under tension (c) Pocket under compression

Fig. 10. Haptic Simulation of Fluid Enclosures In a 2D Environment

tations involved with controlling the haptic device nor displaying graphics to the user. This result only indicates that the iterative solution of the condensed fluid-elastic system can be solved at a rate that is fast enough for haptic applications.

6 Conclusions

This paper presents a technique for modeling fluid-filled structures enclosed by linear elastic media with the Finite Element Method that is fast enough for real-time haptic rendering. By treating hydrostatic fluid pressure as a force boundary condition that acts normal to the fluid-solid boundary, the presence of fluid can be simulated in a simple, yet physically based way. Using a proportional feedback control algorithm that is tuned by numerically investigating the elastic system's response to changes in pressure, a *quasi-static* relationship between the volume and pressure of the fluid structure can be maintained. It is important to note that this method for fast simulation of fluid-filled structures is not limited to use with the FEM. A fluid-filled structure could be added to a deformable object modeled using any method that can accommodate force boundary conditions.

Because the underlying elastic model is linear, computations can be accelerated with matrix condensation techniques. These techniques, along with the optimized pressure-volume understanding, allow for an incompressible fluid pocket to be simulated at 512 Hz as an addition to an existing needle insertion simulation.

The realistic behavior of the method has been validated against an elastic tissue phantom containing an incompressible fluid pocket. Using ultrasound imaging and surface markers for comparison, results from a simulation of the phantom compared well with experimental data up to approximately 15% strain. The accuracy of the method at strains higher than 15% will likely suffer due to the limitations of the linear FEM formulation, as it has limited accuracy at high strain [16].

There are several opportunities for this work to be extended in future research. Firstly, a 3D simulation of surgical techniques that involve avoidance or interaction with fluid pockets could be created using the FEM, fluid modeling, and acceleration methods described in this work. Secondly, the accuracy of these methods could be further validated against other anatomically motivated geometries such as a vein or artery. Thirdly, it would be very interesting to validate the accuracy not only of the deformation, but also of the pressure prediction. A simple experiment with a pressure transducer inside the fluid cavity would yield a good evaluation of the predicted fluid pressure.

References

[1] http://www.ece.ubc.ca/˜andrewg/haptic-fluid-videos/.

[2] M. Agus, A. Giachetti, E. Gobbetti, G. Zanetti, and A. Zorcol. Real-time Haptic and Visual Simulation of Bone Dissection. In *IEEE Virtual Reality*, pages 209–216, 2002.

[3] C. H. An, C. G. Atkeson, and J. M. Hollerbach. *"Model-Based Control of a Robot Manipulator "*. MIT Press, 1988.

[4] R. Balaniuk and K. Salisbury. Dynamic Simulation of Deformable Objects using the Long Elements Method. In *10th Symposium On Haptic Interfaces for Virtual Environments and Teleoperator Systems*, pages 58–65, 2002.

[5] C. Basdogan, C. H. Ho, and M. A. Srinivasan. Simulation of Tissue Cutting and Bleeding for Laparoscopic Surgery Using Auxiliary Surfaces. In *Medicine Meets Virtual Reality*, pages 38–44, 1999.

[6] C. Basdogan, C. H. Ho, and M. A. Srinivasan. Virtual Environments for Medical Training: Graphical and Haptic Simulation of Laparoscopic Common Bile Duct Exploration. *IEEE/ASME Transactions on Mechatronics*, 6(3):269–285, 2001.

[7] J.K. Bathe, H. Shang, and S. Ji. Finite Element Analysis of Fluid Flows Fully Coupled with Structural Interactions. *Computers And Structures*, 72:1–16, 1999.

[8] W. Baxter and M.C. Lin. Haptic Interaction with Fluid Media. In *Proceedings of Graphics Interface*, 2004.

[9] J. Berkley, S. Weghosrt, H. Gladstone, G. Raugi, D. Berg, and M. Ganter. Banded Matrix Approach to Finite Element Modeling for Soft Tissue Simulation. In *Virtual Reality: Research, Development and Application*, volume 4, pages 203–212, 1999.

[10] G. Bianchi, M. Harders, and G. Székely. Mesh Topology Identification for Mass-Spring Models. In *Medical Image Computing and Computer-Assisted Intervention MICCAI 2003*, volume 1, pages 50–58, November 2003.

[11] M. Bro-Nielsen and S. Cotin. Real-time Volumetric Deformable Models for Surgery Simulation using Finite Elements and Condensation. *Proceedings of Eurographics*, 15(3):57–66, 1996.

[12] W. M. Butler. Review of Modern Prostate Brachytherapy. In *Proceedings of the 22nd Annual EMBS International Conference*, pages 748–752, 2000.

[13] R. D. Cook, Malkus D. S., and Pelsha M. E. *Concepts and Applications of Finite Element Analysis*. John Wiley and Sons, 1989.

[14] T. F. Cootes, Taylor C.J., D. H. Cooper, and J. Graham. Active Shape Models - Their Training and Application. *Computer Vision and Image Understanding*, 61(1):38–59, 1995.

[15] Ultrasonix Medical Corp. http://www.ultrasonix.com/.

[16] S. Cotin, H. Delingette, and N. Ayache. A Hybrid Elastic Model allowing Real-time Cutting, Deformations, and Force Feedback for Surgery Training and Simulation. *The Visual Computer*, 16(7):437–452, 2000.

[17] D. d'Aulignac, R. Balaniuk, and C. Laugier. A Haptic Interface for a Virtual Examination of the Human Thigh. In *IEEE International Conference on Robotics and Automation*, pages 2452–2457, 2000.

[18] S. De and M. A. Srinivasan. Thin Walled Models for Haptic and Graphical Rendering of Soft Tissues in Surgical Simulations. In *Medicine Meets Virtual Reality*, pages 94–99, 1999.

[19] H. Delingette. Towards Realistic Soft Tissue Modeling in Medical Simulations. In *Proceedings of the IEEE: Special Issue on Surgery Simulation*, pages 512–523, 1998.

[20] S. P. DiMaio and S. E. Salcudean. Simulated Interactive Needle Insertion. In *10th Symposium on Haptic Interfaces for Virtual Environment and Teleoperator Systems*, pages 344–351, 2002.

[21] S.P. DiMaio, S.E. Salcudean, and M.R. Sirosupour. Haptic Interaction with a Planar Environment. In *9th Symposium on Haptic Interfaces for Virtual Environments and Teleoperator Systems*, pages 1223–1230. International Mechanical Engineering Congress and Exposition (ASME Winter Annual Meeting), 2000.

[22] A. Donangun, A. Durmus, and Y. Ayvaz. Static and Dynamic Analysis of Rectangular Tanks by using the Lagrangian Fluid Finite Element. *Computers and Structures*, 59(3):547–552, 1996.

[23] Y. C. Fung. *"Biomechanics: Mechanical Properties of Living Tissues "*. Springer-Verlag, second edition, 1993.

[24] S. F. F. Gibson. 3D ChainMail: A Fast Algorithm for Deforming Volumetric Objects. Technical Report TR-96-22, MERL - A MITSUBISHI ELECTRIC RESEARCH LABORATORY, http://www.merl.com, 1996.

[25] S. F. F. Gibson and B. Mirtich. A Survey of Deformable Modeling in Computer Graphics. Technical Report TR-97-19, MERL - A MITSUBISHI ELECTRIC RESEARCH LABORATORY, http://www.merl.com, 1997.

[26] H. B. Gladstone, G. J. Raugi, D. Berg, J. Berkley, S. Weghorst, and M. Ganter. Virtual Reality for Dermatologic Surgery: Virtually a Reality in the 21st Century. *Journal of the American Academy of Dermatology*, 42(1):106–112, 2000.

[27] T.J. Hall, M. F. I. Bilgen, and T. A. Krouskop. Phantom Materials for Elastography. *IEEE Transactions on Ultrasonics, Ferroelectrics and Frequency control*, 44(6):1355–1365, 1997.

[28] D. L. James and D. K. Pai. A Unified Treatment of Elastostatic Contact Simulation for Real Time Haptics. *Haptics-E*, 2(1):1–13, 2001.

[29] J. Kim, S. De, and Srinivasan M. A. Physically Based Hybrid Approach in Real Time Surgical Simulation with Force Feedback. In *Medicine Meets Virtual Reality*, pages 158–164, 2003.

[30] B. Mirtich. Fast and Accurate Computation of Polyhedral Mass Properties. *Journal of Graphics Tools*, 1(2), 1996.

[31] D.W. Rickey, P. A. Picot, D. A. Christopher, and A. Fenster. A Wall-Less Vessel Phantom for Doppler Ultrasound Studies. *Ultrasound in Medicine and Biology*, 21(9):1163–1176, 1995.

[32] R. Rohling, P. Munger, J. M. Hollerbach, and T. Peters. Comparison of Relative Accuracy Between a Mechanical and an Optical Position Tracker for Image-Guided Neurosurgery. *Journal of Image Guided Surgery*, 1:30–34, 1995.

[33] J. Sciarretta, A. Samani, J. Bishop, and D. B. Plewes. MR Validation of Soft Tissue Mimicing Phantom Deformation as Modeled by Nonlinear Finite Element Analysis. *Medical Physics*, 29(1):65–72, 2002.

[34] A. Shiraz-Adl and S. C. Shrivastava. Large Deformation Finite Element Treatment of Changes in the Volume of Fluid-Filled Cavities Enclosed in a Structure. *Computers and Structures*, 34(2):225–230, 1990.

[35] Y. Zhuang and J. Canny. Haptic Interaction with Global Deformations. In *IEEE International Conference on Robotics and Automation*, pages 2428–2433, 2000.